An Instrument to Measure Coronal Emission Line Polarization

**S. Tomczyk · G.L. Card · T. Darnell · D.F. Elmore ·
R. Lull · P.G. Nelson · K.V. Streander · J. Burkepile ·
R. Casini · P.G. Judge**

Abstract We have constructed an instrument to measure the polarization of light emitted by the solar corona in order to constrain the strength and orientation of coronal magnetic fields. We call this instrument the Coronal Multichannel Polarimeter (CoMP). The CoMP is integrated into the Coronal One Shot coronagraph at Sacramento Peak Observatory and employs a combination birefringent filter and polarimeter to form images in two wavelengths simultaneously over a $2.8R_\odot$ field of view. The CoMP measures the complete polarization state at the 1074.7 and 1079.8 Fe XIII coronal emission lines, and the 1083.0 nm He I chromospheric line. In this paper we present design drivers for the instrument, provide a detailed description of the instrument, describe the calibration methodology, and present some sample data along with estimates of the uncertainty of the measured magnetic field.

1. Introduction

Coronal physics has progressed enormously over the last decade with the advent of new observations from ground- and space-based instruments. However, many critical questions regarding the structure, heating, and dynamics of the corona will remain open until we can reliably and routinely measure the properties of coronal magnetic fields. Most solar activity, including high-energy electromagnetic radiation, solar energetic particles, flares, and coronal mass ejections, derives its energy from coronal magnetic fields. The corona is also the source of the solar wind with its embedded magnetic field that engulfs the Earth. These phenomena are collectively responsible for perturbations on the Earth's environment known as space weather that affect communications, space flight, and power transmission. Measuring magnetic fields in the solar corona is a necessary step towards understanding and predicting the Sun's generation of space weather.

Radio techniques have been used for several decades to measure coronal magnetic fields. Both thermal bremsstrahlung (Bogod and Gelfreikh, 1980; Ryabov *et al.*, 1999) and thermal

S. Tomczyk (✉) · G.L. Card · T. Darnell · D.F. Elmore · R. Lull · P.G. Nelson · K.V. Streander ·
J. Burkepile · R. Casini · P.G. Judge
High Altitude Observatory, NCAR, P.O. Box 3000, Boulder, CO 80307-3000, USA
e-mail: tomczyk@ucar.edu

gyroresonance emission (Gary and Hurford, 1994; Brosius and White, 2006; see White and Kundu, 1997 for a review) mechanisms have been applied to coronal magnetic field measurements. The gyroresonance mechanism is limited to coronal fields greater than 200 G generally associated with active regions. Faraday rotation from occultation by natural radio sources (Sofue *et al.*, 1976; Mancuso and Spangler, 2000) and by spacecraft (Stelzried *et al.*, 1970) offers the possibility of precise measurements of coronal magnetic fields, however, the use of this technique is hampered by sparse sampling due to the limited availability of sources.

Early work on the measurement of the linear polarization of coronal emission lines at visible and infrared (IR) wavelengths was successful in mapping the direction of coronal magnetic fields (Mickey, 1973; Querfeld and Smartt, 1984; Arnaud and Newkirk, 1987). Circular polarization measurements employing the Zeeman effect can constrain the line-of-sight (LOS) strength of coronal magnetic fields. Despite the nearly four decades since the detection of the Zeeman effect of the coronal green line (Harvey, 1969), coronal Zeeman measurements have not been productive until recently due to advances in the technology of near-IR detector arrays (Lin, Penn, and Tomczyk, 2000; Lin, Kuhn, and Coulter, 2004).

The theory of coronal emission line polarization has been well developed (Charvin, 1965; Hyder, 1965; House, 1972, 1977; Sahal-Bréchot, 1974a, 1974b, 1977). Recent work (Judge, 1998; Casini and Judge, 1999; Judge *et al.*, 2001; Judge, Low, and Casini, 2006) supports the argument that the IR forbidden emission lines hold the greatest promise for the measurement of coronal magnetic fields, due primarily to the λ^2 dependence of the Zeeman shift.

Motivated by these recent technological and theoretical advances, we pursued the development of instrumentation for the measurement of coronal magnetic fields using the Zeeman and Hanle effects of IR emission lines. This paper describes the design and construction of a wide field-of-view (FOV) tunable filter/polarimeter for the measurement of the polarization of the near-IR 1074.7 and 1079.8 nm Fe XIII coronal emission lines and the 1083.0 nm He I chromospheric emission line. The instrument design drivers are discussed in Section 2. A detailed description of the instrument is given in Section 3. The methodology for the polarimetric calibration of the instrument is presented in Section 4. The capabilities of the CoMP instrument are demonstrated with some sample data in Section 5.

2. Instrument Design Drivers

Magnetic fields in the corona are relatively weak, and the emission lines are broad due to the million-degree plasma. The Zeeman shifts associated with coronal magnetic fields are a small fraction of the linewidth. The weak field limit of the Zeeman effect applies and the instrument can be viewed as a coronal magnetograph. The Zeeman effect is encoded in the circular polarization, or Stokes V profile, which in the weak field limit has a wavelength dependence that is proportional to the first derivative of the intensity, Stokes I, profile. The amplitude of the Stokes V signal for the 1074.7 nm coronal line is approximately 10^{-4} of the intensity for a 1 G field (*e.g.* Lin, Kuhn, and Coulter, 2004). This small signal is responsible for the extremely difficult nature of this measurement.

The linear polarization of forbidden coronal emission lines observed in the Stokes Q and U profiles is dominated by resonance scattering, not the usual second-order Zeeman effect seen in most photospheric absorption lines. It has a signal that is $\sim 1 – 10\%$ of the intensity (*e.g.* Arnaud and Newkirk, 1987), so it is orders of magnitude larger than the V signal and has a wavelength dependence that is proportional to the Stokes I profile. For magnetic fields typical in the solar corona, the Hanle effect is saturated in the 1074.7 and 1079.8 nm Fe XIII

lines. In this regime the Stokes Q and U observations cannot constrain the strength of the transverse component of the magnetic field, but can only constrain the plane-of-sky (POS) direction of the field.

In the weak field regime, a coronal magnetograph can constrain the LOS field strength and POS field direction with observations at line center and in each of the line wings. With the requirement of only a few spectral samples, a filter instrument offers a significant multiplexing advantage over a spectrograph instrument, and was chosen for this application. Even with three passbands, LOS velocities can be determined from the Doppler shift of the emission line, and a coronal density diagnostic can be obtained from the ratio of the Fe XIII 1074.7/1079.8 lines (Penn *et al.*, 1994).

Since the coronal Stokes V measurement is much more difficult than Q or U, we have selected the filter bandpass for optimal V sensitivity following the formulation of Babcock (1953). For a constant line intensity, the signal-to-noise ratio for a magnetic field measurement is proportional to the ratio of the Stokes V signal integrated over the filter bandpass, divided by the square-root of the line intensity plus background integrated over the filter (assuming photon noise):

$$S/N \propto \frac{\int_\lambda V(\lambda, w) F(\lambda, \Delta\lambda, d) \, \mathrm{d}\lambda}{(\int_\lambda (I(\lambda, w) + B) F(\lambda, \Delta\lambda, d) \, \mathrm{d}\lambda)^{\frac{1}{2}}}. \tag{1}$$

To determine the optimal filter width and displacement into the line wing, we have evaluated Equation (1) assuming that the line intensity profile is Gaussian, the background, B, is constant with wavelength, and the Stokes V profile is given by the first derivative of a Gaussian. Here w is the line e-folding half width which is assumed to have a value of 0.107 nm (30 km s^{-1}) for the 1074.7 nm line, $\Delta\lambda$ is the filter FWHM, and d is the displacement of the filter bandpass into the line wing. The filter transmission profile, F, was modeled using an analytical expression for a four-stage birefringent filter (Billings, 1947), required to provide a sufficient free spectral range. Equation (1) was evaluated as a function of the filter width and displacement for two cases (Figure 1). The first case assumes no background, and the other case assumes background dominated observations with a background level ten times the peak line intensity. Optimal values of the filter width and displacement are evident in Figure 1, however, the maxima are quite broad, especially in the filter FWHM. For the $B = 0$ case, optimal values are $\Delta\lambda = 0.161$ nm and $d = 0.134$ nm; for the $B = 10 I_{\text{peak}}$ case, optimal values are $\Delta\lambda = 0.117$ nm and $d = 0.088$ nm. Since our filter will be tunable, one can select the position of the filter bandpasses for the given observing conditions, however, the filter width must be fixed during the design of the filter. The no-background case is applicable to space based observations. For ground-based observations we expect conditions to be intermediate between the two cases shown, so we have selected a value for the filter FWHM of 0.13 nm.

Due to their capabilities for wide-field imaging and multiple beam output, combined with our experience with a filter for He I 1083 nm imaging (Kopp *et al.*, 1997), we have chosen to build an instrument with the following characteristics: (1) Four-stage calcite wide-field birefringent filter with liquid crystal tuning, operating at 1074.7, 1079.8, and 1083.0 nm; (2) filter bandpass of 0.13 nm FWHM; (3) liquid crystal polarization analysis for complete Stokes *I, Q, U, V* measurement; (4) polarizing beamsplitter for simultaneous measurement of line and continuum; (5) high quantum efficiency IR imager; and (6) a large coronal FOV. The details of the instrument are described in the next section.
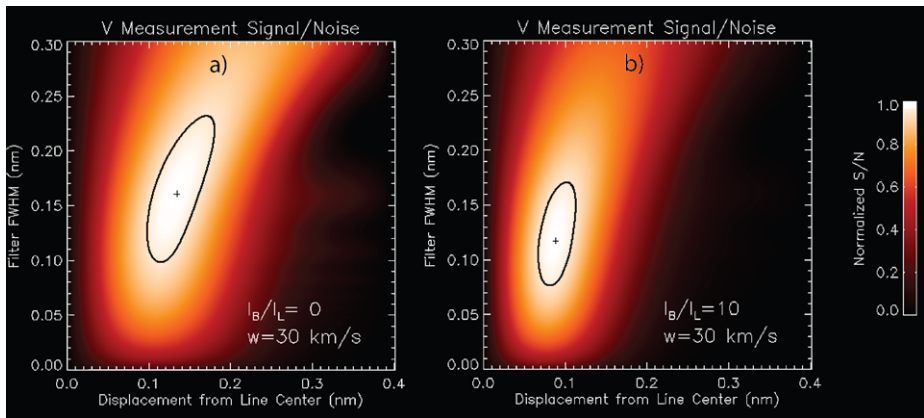
Figure 1 Normalized signal-to-noise ratio of the Stokes *V* measurement as a function of the filter FWHM and the displacement of the filter bandpass away from line center, assuming an e-folding line width of the emission line of 0.107 nm. (a) The case for no background light. (b) The case for a background dominated measurement with the background light level a factor of ten greater than the emission line intensity. The point of maximum S/N is indicated by the cross and the contour encloses the region of normalized S/N greater than 0.95.

3. Instrument

3.1. Coronagraph and Optical System

The CoMP instrument was integrated into the Coronal One Shot coronagraph (COS; Smartt, Dunn, and Fisher, 1981) mounted on the equatorial spar at the Hilltop facility at the Sacramento Peak Observatory of the National Solar Observatory. The COS was built and operated in the early 1980s for photographic observation of the coronal green line (530.3 nm), coronal red line (637.4 nm), Hα (656.3 nm) on the solar disk and Hα above the limb. The One Shot name is derived from the capability to image the entire corona in a single exposure. The COS objective lens is a 20-cm aperture uncoated BK7 biconvex f/11 singlet. The front surface of the lens is aspheric. The lens has been polished to coronagraphic quality; scattered light from this lens was measured (Smartt, 1979) to be about 3 $\mu B_\odot$ (where $\mu B_\odot$ are units of one millionth of the solar disk central intensity) at 0.28° off axis in white light. The coronagraph was designed to allow easy removal of the primary to facilitate cleaning. The telescope tube is lined with light-trapping hexagonal aluminum core material. A lens cover is located 46 cm in front of the objective lens. The back end of the COS including the original occulting disk assembly, birefringent filter, and transfer optics were replaced by the corresponding components of the CoMP.

The CoMP optical system is shown in Figure 2. It consists of the 20-cm COS objective lens (not shown in the figure), an occulting disk at the prime focus, a collimating lens, a filter wheel containing the three prefilters, the birefringent filter, and a reimaging lens, followed by the detector. The collimating lens is comprised of two stock 600 mm focal length lenses forming a 300 mm focal length f/5 lens, while the reimaging lens is a stock Mamiya R22 110 mm focal length, f/2.8 camera lens. This lens is superior in image quality to a custom lens we built for this purpose. The only shortcoming of the Mamiya lens is that its anti-reflection coatings are not optimized for the near-IR. It has a transmission of 0.66 at 1064 nm. The reimaging lens forms simultaneous images of the line and continuum over a 2.8$R_\odot$ full FOV with 4.5 arcsec pixel^{-1} sampling.
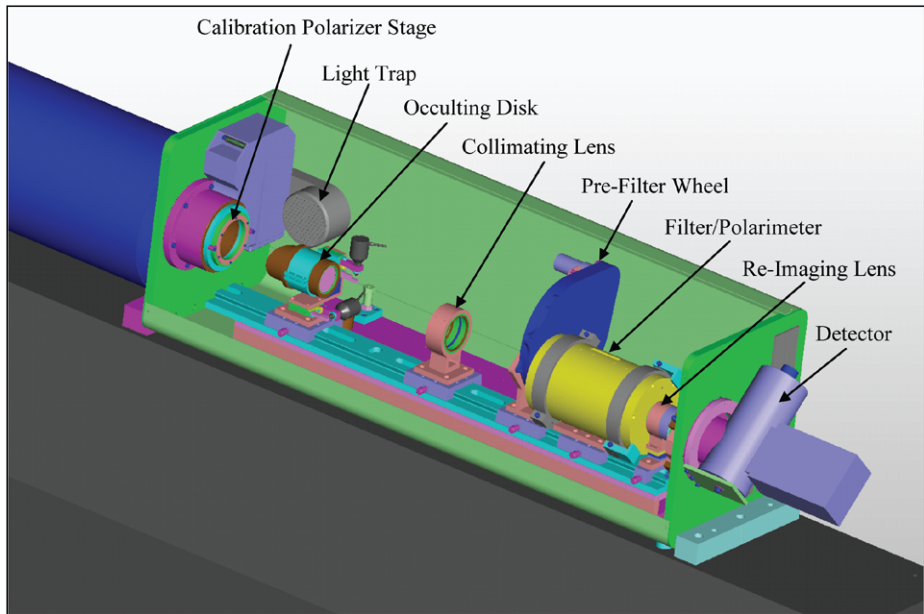
Figure 2 Solid model rendering of the CoMP instrument package. Colors are for clarity only. Light enters through the blue tube on the left.

Chromatism of the singlet objective lens causes its focal distance to change by 0.49 mm over the wavelength range of 1074.7 to 1083.0 nm. This change is smaller than the 1.06 mm depth of focus assuming a blur size equal to our spatial sampling of 4.5 arcsec. Since all the other lenses are achromats, no refocusing is needed over the entire wavelength range.

We use the original COS diamond-polished aluminum occulting disks which are available in a range of diameters to accommodate the changing solar image size throughout the year. An angled reflector slightly smaller in diameter located directly in front of the occulting disk reflects most of the light from the solar disk to a light trap. The occulting disk and reflector are held in the beam by a single thin vane. A circular field stop limits the FOV to $2.8R_\odot$.

The collimating lens forms an image of the objective on a Lyot stop which is located inside the birefringent filter. The circular stop consists of deposited aluminum on a glass substrate and is inserted into the stack of elements that comprise the birefringent filter (described in the next section). The Lyot stop has a radius of 12.7 mm which is a factor 0.93 of the radius of the projected image of the objective lens. This causes a reduction in the scattered light from diffraction around the objective lens by a factor of approximately 5×10^{-5} (Noll, 1973; Johnson, 1987) which renders this source of light negligible.

We have not included a "Lyot spot" to block the spurious image produced by multiple reflections in the objective lens. This image has a brightness of $B \approx 6 \times 10^{-9}(f/\#^2)B_\odot$ (Newkirk and Bohlin, 1963) where $f/\#$ is the f-number of the system. For our system, this amounts to 7×10^{-7} $B_\odot$. This is significantly smaller than the typical sky brightness at Sacramento Peak.

3.2. Filter/Polarimeter

We selected a birefringent filter design for this instrument due to the wide-field capability, and the ability to provide multiple output beams. The adopted design is a four-stage calcite
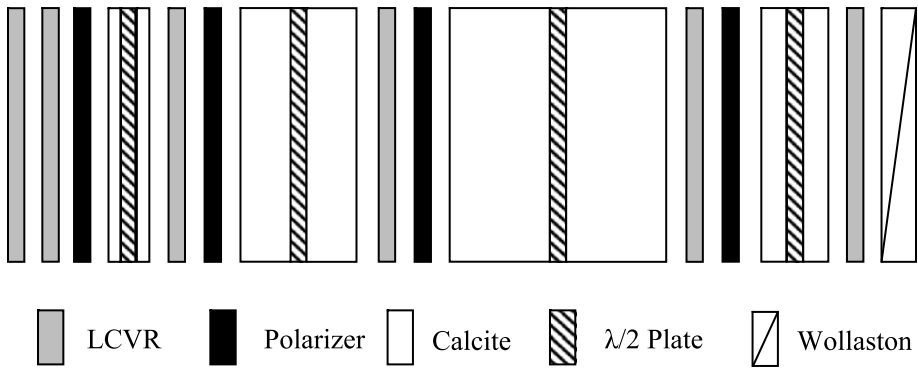
Figure 3 Diagram of the optical components of the filter/polarimeter. The identification of the elements is indicated below. Light enters from the left. Dimensions are not to scale, except for relative thicknesses of calcite elements.

birefringent filter (Lyot, 1944; Evans, 1949). The exit polarizer is replaced by a Wollaston polarizing beamsplitter (Öhman, 1956) allowing simultaneous imaging in the line and continuum. Each of the calcite stages is in a wide field configuration and has a corresponding Nematic Liquid Crystal Variable Retarder (LCVR) for tuning. Two LCVRs are located before the first polarizer for the analysis of the input polarization state. The optical elements comprising the filter/polarimeter are shown in Figure 3. Interference filters with a full width of ∼ 1.7 nm are used to block the unwanted orders of the birefringent filter for each emission line.

Many researchers have employed Nematic LCVRs for the tuning of birefringent filters (Tarry, 1975; Wu, 1989; Miller, 1990; November and Wilkins, 1992; Kopp, 1994; Staromlynska, Rees, and Gillyon, 1998; Wang *et al.*, 2001). For beam separation, we employ a calcite Wollaston prism with a cut angle of 15°. The polarizers are Corning Polarcor and have a transmission of 0.97 to polarized light and a contrast ratio in excess of 10^4. The half-waveplates are polymer retarders sandwiched between glass substrates.

The birefringent filter was designed using Jones matrix algebra following the formulation of Beckers and Dunn (1965). The filter bandpass was chosen to be 0.13 nm as described in Section 2. The free spectral range is 2.34 nm. Rotational misalignment of the elements of a birefringent filter results in an increase in the filter transmission outside of the main transmission band. The dependence of this parasitic transmission to the angular orientation of filter elements was evaluated by performing a Monte Carlo simulation where many theoretical realizations of the filter transmission profile were computed with the filter elements having varying degrees of angular misalignment. This simulation indicated that the calcite elements are much more sensitive to angular misalignment than the other elements and their orientation needs to be maintained to better than 0.5° rms. Angular orientation of the optical components is maintained by mounting the elements in octagonal aluminum holders. Precise angular alignment was achieved by rotating the elements in an alignment jig for minimum transmission between crossed reference polarizers before adhering the elements to the holder with Silicone RTV. We estimate the accuracy of angular orientation to be better than 0.1°.

Figure 4 shows an exploded view of the filter/polarimeter. All optical elements are uncoated with the exception of the outside surfaces of the entrance and exit windows. Reflective losses are minimized by inserting a layer of high viscosity optical oil (Dow Corning 200 Silicone oil 10 000 cSt) with a refractive index of 1.4 between the optical elements. The
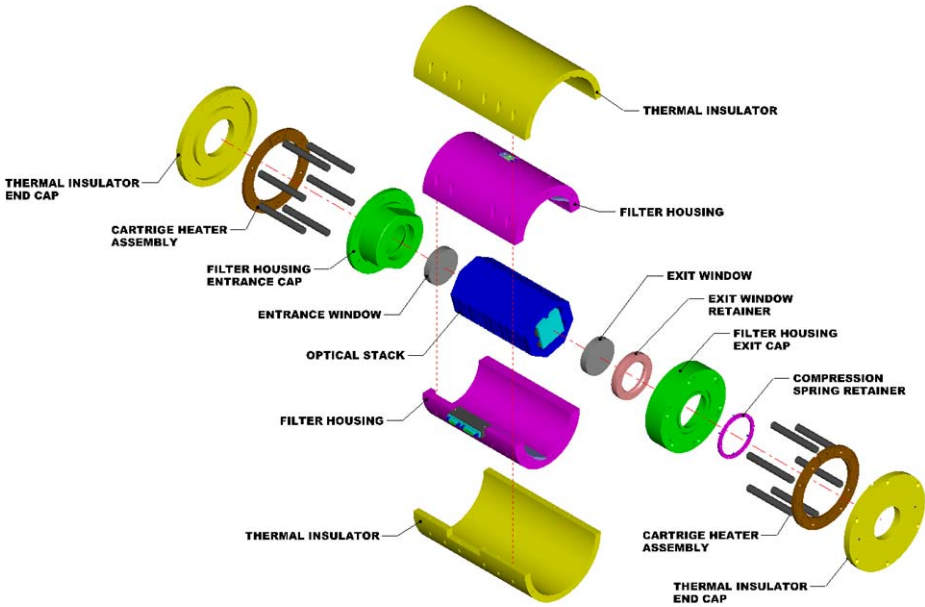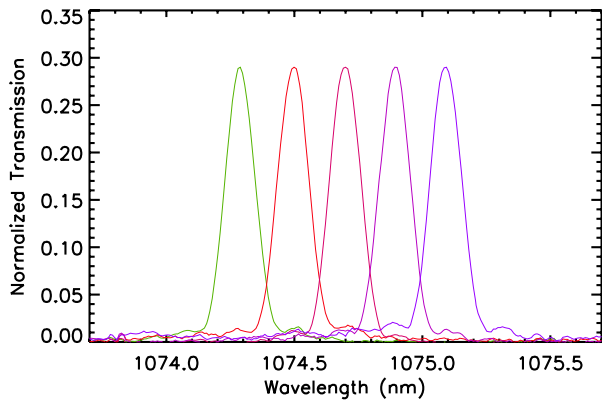
Figure 4 Exploded view of the filter/polarimeter. Colors are for display purposes only.

Figure 5 Measurement of the transmission profile of the tunable filter to input unpolarized light in the vicinity of the 1074.7 nm line. Five tunings are shown, each shifted by 0.2 nm.

elements are kept in contact by the application of ~ 5 lbs of force applied to the periphery of the exit/entrance windows by a set of springs through an o-ring.

Transmission profiles of the birefringent filter measured with a spectrograph are shown in Figure 5. The maximum transmission of the filter to unpolarized light is 0.29 (out of a maximum of 0.5). The primary contribution to the transmission losses are the transmission of the six LCVRs and the four polarizers which are 0.96 and 0.98 each respectively at 1074 nm. The complete filter/polarimeter including optics, aluminum housing, and Delrin insulation layer have a total weight of 5.5 kg.

3.3. Detector

The detector is a Rockwell Scientific TCM8600 HgCdTe 1024×1024 array with 18 µm square pixels. The readout noise has been measured to be $70e^-$ and the useful full well depth is about $150\,000e^-$. The data are digitized to 14 bits at the camera using eight output channels with a conversion factor of $\sim 25e^-$ per least significant bit. The camera can be read out at a rate of 30 Hz. The camera is cooled with liquid nitrogen and has a hold time of about 12 hours. An identical detector and electronics have demonstrated excellent linearity characteristics (Cao *et al.*, 2005).

3.4. Intensity Calibration

In order to calibrate the intensity of our images, a diffuser can be inserted in front of the objective under computer control. The diffuser is a 40° FWHM holographic light shaping diffuser (LSD). Assuming a Gaussian scattering distribution that is typical for holographic LSDs, the diffused beam is uniform in intensity over our FOV to a few parts in 10^4. Normalization by the diffuser images performs four functions:

1. Flat-fielding to remove pixel-to-pixel detector sensitivity variations.
2. Normalization of filter transmission variation with wavelength due primarily to the pre-filter.
3. Relative normalization of the two beams.
4. Normalization of the intensity to disk intensity units.

The diffuser has been calibrated to disk-intensity units by comparing an observation taken with the diffuser to an observation of the solar disk through a neutral density filter in front of the objective lens. The transmission of the ND filter was measured to be 3.0×10^{-5} at 1064 nm resulting in a calibrated radiance of the diffuser of 84 $\mu B_\odot$.

3.5. Temperature Control

The temperature sensitivity of the filter/polarimeter is dominated by the temperature dependence of the birefringence of the calcite, with the temperature dependence of the LCVR retardance a much smaller effect. Modeling of the filter indicates a temperature shift of the filter bandpass of -0.056 nm C^{-1} (-15.6 km s^{-1} C^{-1}). Stabilization of the filter is achieved through nested temperature control loops, the first maintaining the temperature of the instrument enclosure and the second maintaining the temperature of the filter itself.

The instrument enclosure is insulated and maintained at a constant temperature of 35° C to within about one degree by a PID temperature servo driving Kapton Thermofoil resistive heaters. The heaters are capable of 110 W and are attached to 90% of the surface area of the bottom of the plate which supports the instrument optical system. The birefringent filter is maintained at a temperature of 30° C by 12 cartridge heaters located in the filter housing (Figure 4). These Inconel heaters are wired in parallel each with a 45-W capacity. They are controlled by a precision PID controller that maintains the temperature stability of the birefringent filter to better than 5 mC over a time scale of 24 hours.

RTD temperature sensors are located on the optical components inside the filter assembly, in the optics enclosure, and in the electronics rack in order to monitor the temperature stability and to evaluate thermal gradients. These sensors are independently logged by a temperature sensing unit.

3.6. Data Acquisition

The control computer is a Pentium 4 PC running Windows 2000. The instrument control software was written in LabView and allows control of all instrument functions including: inserting and removing the diffuser, opening and closing the lens cover, translating the occulting disk, positioning the filter wheel, application of LCVR control voltages, focusing the reimaging lens, and all camera control functions. The camera is interfaced to the control computer through a Camera Link interface. The instrument can be operated manually or in an automated mode where a list of observations at various wavelengths and polarization states can be obtained. The block diagram for the CoMP instrument is illustrated in Figure 6.

4. Polarimetric Calibration

In order to convert the measured Stokes vectors into real Stokes vectors, we must calibrate the instrument by observing the response to known input Stokes states. The polarimetric response of the instrument can be written as

$$\mathbf{S}_{\mathrm{meas}} = \mathbf{R}\mathbf{S}_{\mathrm{input}}, \tag{2}$$

where $\mathbf{S}_{\mathrm{input}}$ is the Stokes vector input into the polarimeter, $\mathbf{S}_{\mathrm{meas}}$ is the measured Stokes vector, and $\mathbf{R}$ is the 4×4 element response matrix which relates the two. An ideal polarimeter will have a response matrix that approaches the unity matrix; off-diagonal elements represent crosstalk between Stokes states.

For calibration the diffuser is placed in front of the objective lens. Linearly polarized light is produced by inserting a linear polarizer on a rotation stage located in front of the occulting disk assembly, while circularly polarized light is produced by inserting a stationary quarter-wave plate immediately behind the linear polarizer. The linear polarizer is a Versalight reflective wire grid polarizer and the quarter-wave plate is a true zero-order polymer waveplate between glass substrates.

To determine the elements of the response matrix, a sequence of data is taken of the Sun through the diffuser: (1) without the calibration polarizer and waveplate in the beam which inputs approximately unpolarized light into the polarimeter; (2) with the calibration polarizer in the beam at angles of $0°$, $45°$, $90°$, and $135°$ which inputs Stokes $I + Q$, $I + U$, $I - Q$, and $I - U$ into the polarimeter; (3) with the calibration retarder fixed at $0°$ and the calibration polarizer at $+/-45°$ which inputs Stokes $I + / - V$.

These data are analyzed by a nonlinear least-squares routine that uses a model to solve for the following 23 quantities: the transmission of the calibration polarizer, the transmission of the calibration retarder, the four components of the Stokes vector input during the calibration process, the retardation of the calibration retarder, the angular error in the orientation of the calibration waveplate, and the elements of the response matrix excluding the 1, 1 term that is normalized to have a value of 1. These parameters have been determined for each pixel over the FOV. The spatially averaged values for the response matrix elements are

$$\mathbf{R} = \begin{bmatrix} 1.000 & -0.026 & -0.014 & -0.005 \\ -0.005 & 0.952 & -0.002 & 0.046 \\ 0.002 & -0.004 & 0.977 & -0.056 \\ -0.001 & -0.018 & -0.048 & 0.876 \end{bmatrix}. \tag{3}$$
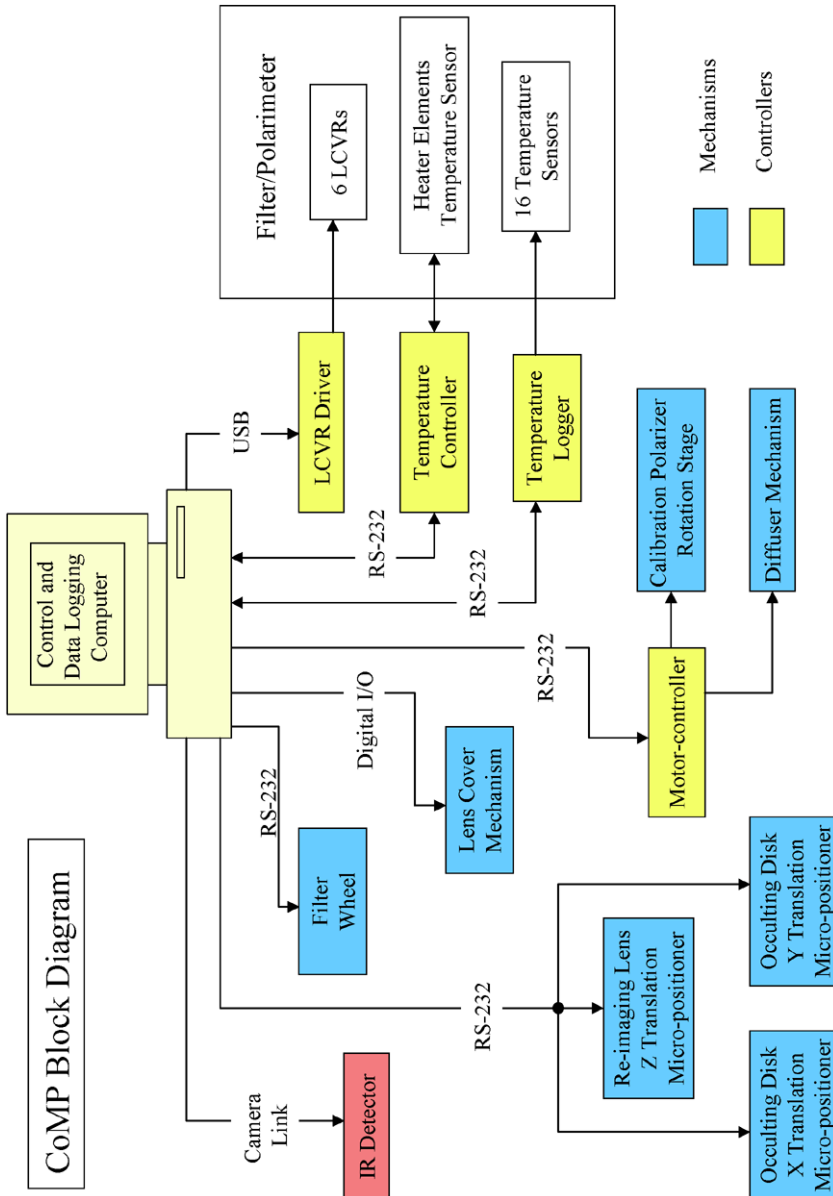
Figure 6 Block diagram of the CoMP instrument.

To smooth out high spatial frequency variations in the inferred response matrix and to parameterize its spatial variation, each of the response matrix elements have been fit with a low-order polynomial in the two spatial dimensions. Application of the response matrix follows from evaluation of the response matrix at a given pixel from the low-degree fit, computing the inverse of the response matrix, and calculating the input Stokes vector from the measured Stokes vector from the inverse of Equation (2):

$$\mathbf{S}_{\text{input}} = \mathbf{R}^{-1}\mathbf{S}_{\text{meas}}. \tag{4}$$

The requirement on the accuracy of the knowledge of the response matrix can be determined by considering the expected signals from the corona and the observational requirements. Given expected values for the linear polarization of up to about 10% and a magnetic field strength of 10 G, the Stokes vector from the corona has a magnitude of order:

$$\mathbf{S}_{\text{corona}} \approx \begin{bmatrix} 1 \\ 0.1 \\ 0.1 \\ 10^{-3} \end{bmatrix} I. \tag{5}$$

The acceptable uncertainty for calibrated Stokes vectors is set by our desire to observe I, Q/I, and U/I to an accuracy of 10^{-3} and to observe Stokes V/I to an equivalent precision of 1 G corresponding to a signal of 10^{-4} for the Fe XIII 1074.7 nm line. This gives a desired Stokes noise vector:

$$\boldsymbol{\sigma}_{\mathbf{S}} \leq \begin{bmatrix} 10^{-3} \\ 10^{-3} \\ 10^{-3} \\ 10^{-4} \end{bmatrix} I. \tag{6}$$

Then, using Equation (2) with $\mathbf{S}_{\text{corona}}$ for the input and $\boldsymbol{\sigma}_{\mathbf{S}}$ for the output we find that the acceptable errors on the response matrix elements are of order:

$$\boldsymbol{\sigma}_{\mathbf{R}} \leq \begin{bmatrix} - & 10^{-2} & 10^{-2} & 10^{0} \\ 10^{-3} & 10^{-2} & 10^{-2} & 10^{0} \\ 10^{-3} & 10^{-2} & 10^{-2} & 10^{0} \\ 10^{-4} & 10^{-3} & 10^{-3} & 10^{-1} \end{bmatrix}. \tag{7}$$

Since the response matrix is normalized such that the 1, 1 element is unity, the error in that term is not considered.

The precision of the calibration methodology was evaluated through a Monte Carlo simulation. Data sets were created with random values of the above set of 23 unknowns. The data sets were then fit with the least-squares procedure and the inferred parameters compared to the input ones. A simulation with 1000 realizations was used to estimate the errors in the determined values of the response matrix, which are:

$$\boldsymbol{\sigma}_{\mathbf{R}} = \begin{bmatrix} - & 1.07\text{e}-3 & 1.16\text{e}-3 & 2.92\text{e}-3 \\ 6.86\text{e}-4 & 8.24\text{e}-4 & 9.19\text{e}-4 & 2.73\text{e}-3 \\ 5.08\text{e}-4 & 8.27\text{e}-4 & 1.12\text{e}-3 & 4.46\text{e}-2 \\ 5.12\text{e}-4 & 7.95\text{e}-4 & 9.21\text{e}-4 & 6.04\text{e}-3 \end{bmatrix}. \tag{8}$$

These errors are for each pixel in the FOV. They are comfortably below the response matrix error requirement of Equation (7), except for the fourth row of the matrix that describes the crosstalk of Stokes I, Q, and U into V. This is due to the stringent noise requirement on Stokes V and implies that for magnetic fields of 1 G or less, the crosstalk from Stokes I, Q, and U will probably dominate the Stokes V signal even after calibration. However, it is possible to use the fact that the Stokes V profile is antisymmetric around line center, while Stokes I, Q, and U are symmetric, to empirically remove crosstalk in the Stokes V measurement. This has been successfully demonstrated in a system with Q and U to V crosstalk of order 10% in the measurement of field strength to a fraction of a Gauss (Lin, Kuhn, and Coulter, 2004).

5. Sample Data

The instrument was deployed on the COS on 29 January 2004. Several subsequent observing runs were devoted to the solution of instrument problems. A time series of CoMP velocity and linear polarization data have been used to observe Alfvén waves in the corona and are presented elsewhere (Tomczyk *et al.*, 2007). To demonstrate the capabilities of the CoMP instrument to measure the polarization of coronal emission lines, we present here data taken on 31 October 2005 in the Fe XIII 1074.7 nm line between 15.04 and 17.46 UT.

The data were obtained in groups of 60 images taken in quick succession in either circular or linear polarization. The linear polarization image groups were comprised of five images taken in each of the four polarization states $I + Q$, $I - Q$, $I + U$, $I - U$, at the three wavelengths 1074.52, 1074.65, and 1074.78 nm, while the circular polarization image groups were comprised of ten images taken in each of the two polarization states $I + V$, $I - V$ at the same three wavelengths. The exposure time for the images was 250 ms and each exposure was followed by a delay of 100 ms to allow for the settling of the LCVRs. The time required to obtain an image group and write it to disk was approximately 29 s. Given that photons were collected for 15 s during each group, the corresponding duty cycle was 52%.

Over the 2.4-hour observing period, 146 circular polarization image groups and 37 linear polarization image groups were collected. Data were also obtained in the Fe XIII 1079.8 nm and the He 1083.0 nm lines during this period, but those data will not be discussed here. The sky conditions were good throughout the observations with a median sky background over the FOV of 16.4 μB$_\odot$.

Initial data reduction steps are: (1) subtract a mean dark image; (2) normalize by a mean image taken with the calibration diffuser; (3) determine the location of the images on the detector, translate to a common center, and rotate to orient solar north up; (4) subtract the continuum image from the line image; (5) compute average measured Stokes images at each wavelength for the image group; and (6) correct for polarimeter crosstalk by applying the inverse response matrix.

The Stokes images for all the groups were averaged over the observing period and a sub-array of the data on the east-limb was selected for analysis. Figure 7 shows an image of the average intensity of the corona in Fe XIII 1074.7 over this period superposed with a contextual Hα image of the solar disk obtained with the HAO PICS instrument at Mauna Loa. The selected subarray subtends approximately $0.4 \times 0.7 R_\odot$ and is indicated by the white box over the east limb. For each pixel in this region we performed a nonlinear least-squares fit to the data simultaneously in the four Stokes parameters at the three wavelengths. The fit model assumed that the I, Q, and U profiles were Gaussian in shape and that the V

Figure 7 Image of the intensity of the corona above the limb in the Fe XIII 1074.7 nm emission line along with a simultaneous Hα image on the solar disk for context. The subarray selected for analysis is shown as the box over the east limb. The lower limit of coronal data is $1.05 R_\odot$.
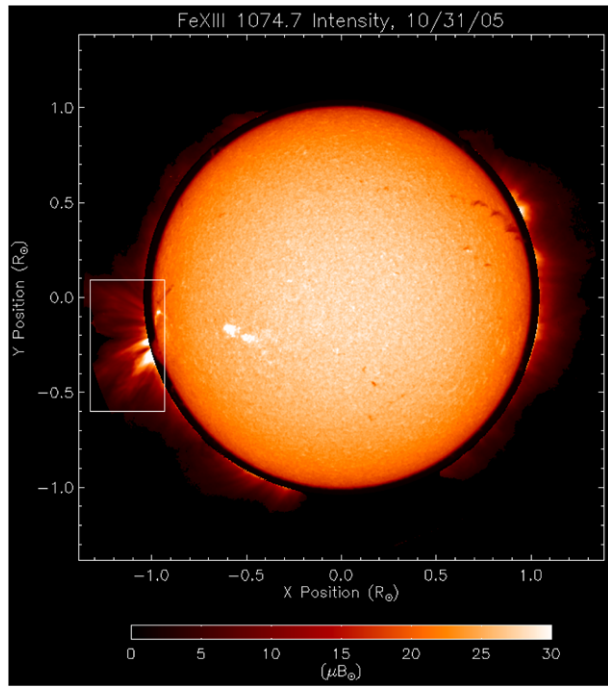
profile is given by the first derivative of a Gaussian. The following seven parameters were fit at each point: the line center intensity, line width, center wavelength, degree of linear polarization, $p = (Q^2 + U^2)^{1/2}/I$, azimuth of the magnetic field, $\phi = 0.5 \arctan(U/Q)$, and a parameter to remove the symmetric Gaussian component from the V signal due to residual crosstalk from I, Q, or U into Stokes V (see also Lin, Kuhn, and Coulter, 2004). The fit process included a realistic model of the filter bandpasses.

The results of the fit are shown in Figure 8. The LOS velocity (Figure 8(b)) was obtained from the line center wavelength in the usual way. It shows a significant variation of relative velocity over the fit region. Figure 8(c) illustrates the azimuth of the magnetic field as vectors without direction due to the 180° ambiguity inherent in the linear polarization measurement. Not surprisingly, these vectors follow the loop structures. The LOS magnetic field strength (Figure 8(d)) shows a bipolar structure with the upper part of the region having a negative polarity and the lower part of the region a positive polarity. The height variation of linear polarization averaged over all latitudes is shown in Figure 9 and shows the normal increase with height (*e.g.* Arnaud and Newkirk, 1987).

For this day, the occulting disk size was 27.6 arcsec larger than the solar disk in radius. Typically the three pixels above the occulting disk are subject to excess noise due to image motion and are not used. The resulting lower limit of displayed data in the figures is $1.05 R_\odot$.

Since the formal errors from the fitting process generally underestimate the true errors, we have empirically estimated the error on the LOS magnetic field as follows. The error on the central wavelength of an emission line is (Penn *et al.*, 2004)

$$\sigma_{\lambda_0} = \frac{w}{\sqrt{2}} \frac{\sigma_I}{I}, \tag{9}$$
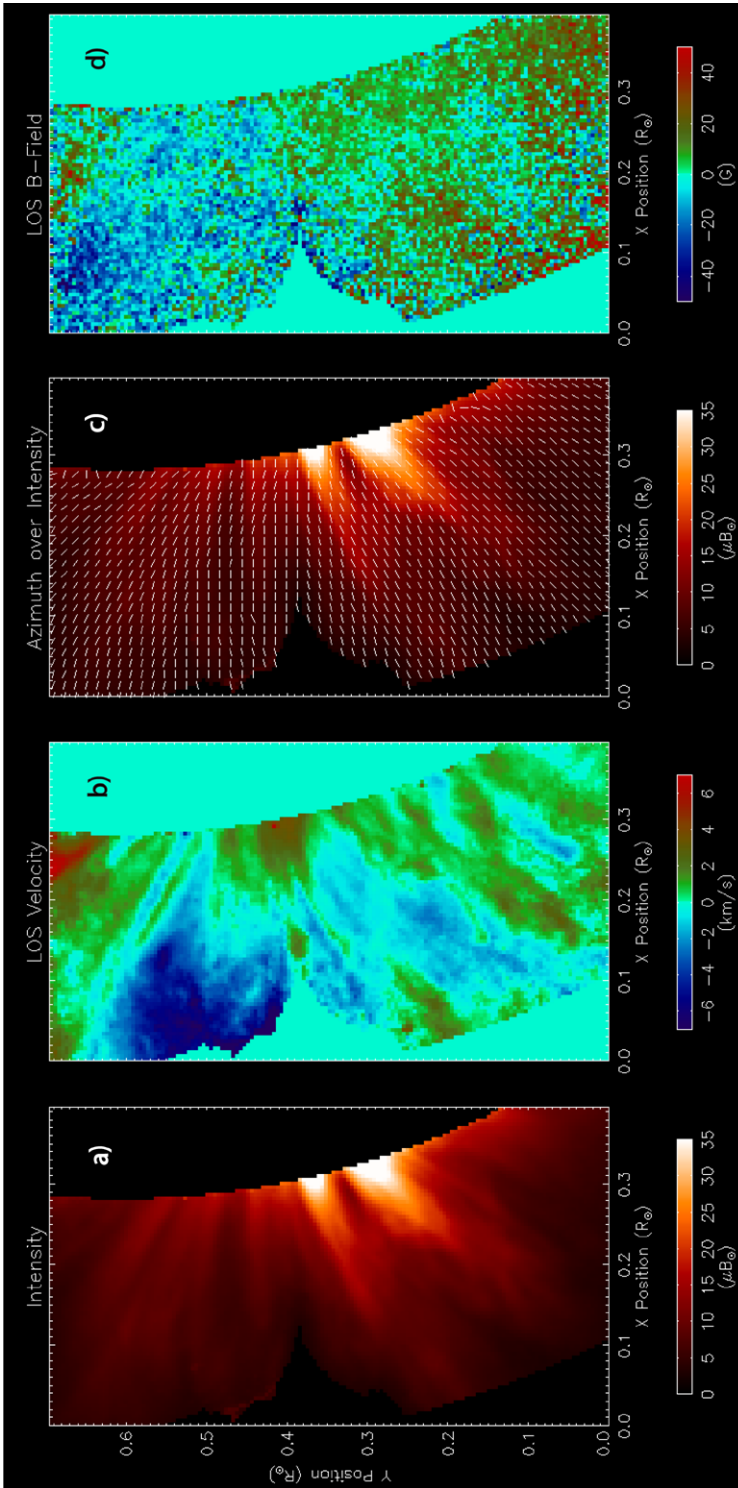
Figure 8 Map of inferred values of coronal parameters over the subarray shown in Figure 7. (a) The intensity of the Fe XIII 1074.7 nm emission line; (b) The LOS velocity; (c) The intensity with superimposed vectors showing the plane-of-sky direction of the magnetic field; (d) The LOS component of the coronal magnetic field.

Figure 9 Variation of the latitudinally averaged linear polarization with height.
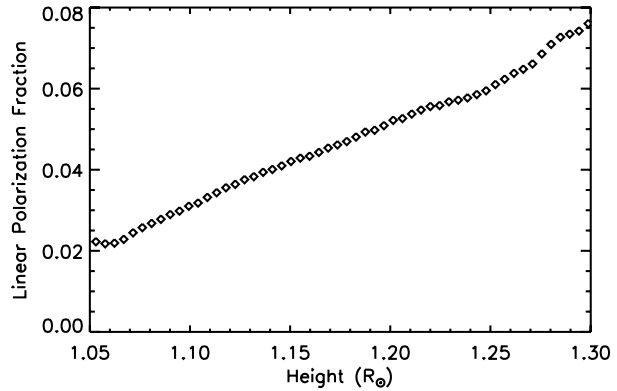
where w is the width of the emission line. To convert this wavelength error into an equivalent error on the LOS magnetic field strength, we use the fact that the Zeeman shift is $4.67 \times 10^{-12} g\lambda^2$ nm G^{-1} (*e.g.* Landi Degl'Innocenti, 1992), where g is the Landé factor. For the 1074.7 nm line, $g = 1.5$ and w has a typical value of 0.107 nm (30 km s^{-1}). Since we measure $I \pm V$ and $V \ll I$, then $\sigma_V \approx \sigma_I$. From this we derive the error on the LOS magnetic field strength of

$$\sigma_B = 9396 \frac{\sigma_V}{I} (G), \tag{10}$$

where σ_V and I are in $\mu B_\odot$. For each pixel in the fit region we empirically determined σ_V by computing the scatter of the V signal among the 146 circular polarization image group samples, and divided the scatter by $146^{1/2}$ since we averaged these samples for the LOS magnetic field determination. We then normalized by the local intensity and computed σ_B through Equation (10). This quantity is shown in Figure 10(a). It shows the errors on the LOS magnetic field are between about 2 and 10 G over the fitted region.

To compare this quantity to the expected error due to photon noise, we have computed the photon noise from the average intensity of each pixel. The uncertainty in photons is $\sigma_N = N^{1/2}$, and we have $N = Ik$, where I is in $\mu B_\odot$ and k is the conversion factor in photons $\mu B_\odot^{-1}$. Using $\sigma_V \approx \sigma_I$ as before, we find that

$$\sigma_V = \frac{\sqrt{I}}{\sqrt{k}}, \tag{11}$$

where σ_V and I are in units of $\mu B_\odot$. To compute the expected σ_V due to photon noise in the average over the observing period, we substitute into Equation (11) the average intensity over the fit region including the additional constant background level of 16.4 $\mu B_\odot$, use the value of $k = 875$ photons $\mu B_\odot^{-1}$, and divide σ_V by $20^{1/2}$ and $146^{1/2}$ since there are $20 V$ images per wavelength in each image group and 146 image groups for the observing period. This quantity is then converted to equivalent expected photon noise error on the LOS magnetic field using Equation (10), and is displayed in Figure 10(b). The error due to photon noise (Figure 10(b)) shows a remarkable correspondence to the error derived from the scatter of the observations (Figure 10(a)). This demonstrates that these observations are photon noise limited, except for those points close to the occulting disk and at the edges of bright features where image motion introduces excess noise in Stokes V. Histograms of the observed and photon noise limited errors are compared in Figure 11. The median error over the fitted region estimated from the Stokes V scatter is 3.5 G compared to the median error
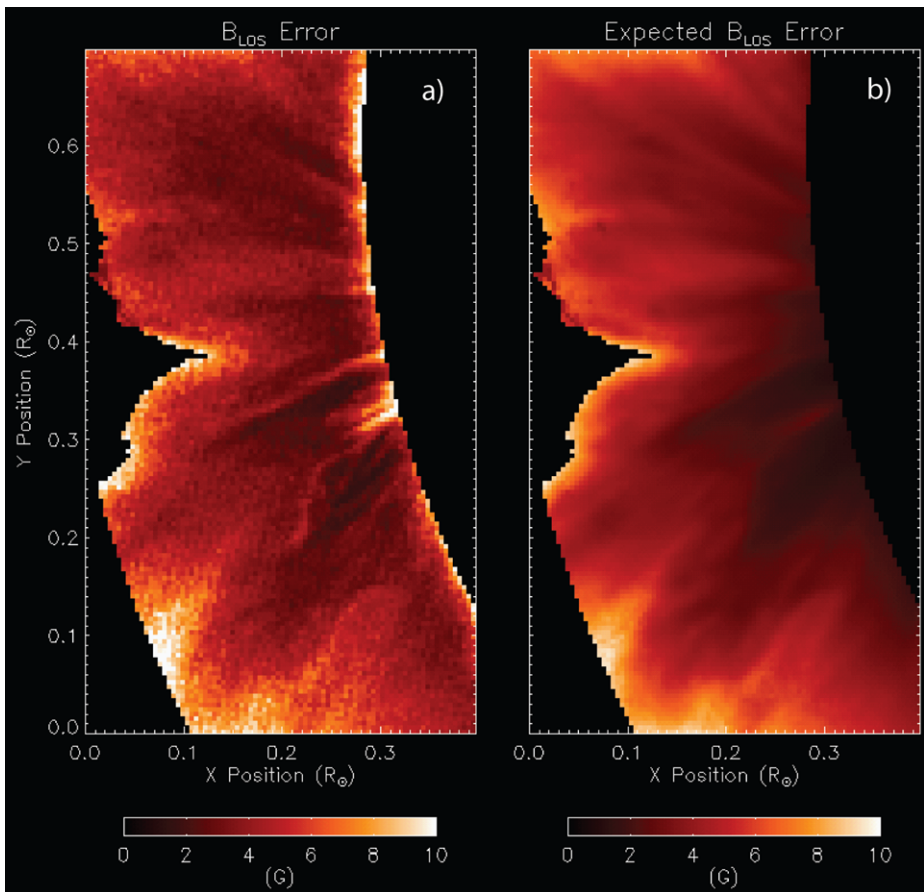
Figure 10 (a) Error on the LOS strength of the magnetic field estimated from the scatter of the Stokes *V* signal. (b) Corresponding estimate obtained from photon noise applied to the intensity signal.

from photon noise of 3.2 G. The observed errors can be reduced by averaging pixels with a corresponding reduction in the spatial resolution.

6. Conclusion and Future Prospects

We have constructed an instrument to measure the polarization of coronal emission lines for the purpose of inferring the properties of coronal magnetic fields. Despite stringent observational requirements, we have designed and constructed an instrument that can achieve near photon noise limited performance. The measured noise level of a few G was achieved with 4.5 arcsec pixels in 2.4 hours of integration using a 20-cm aperture coronagraph with a background level of 16.4 $\mu B_\odot$.

Given that we are photon noise limited, the performance demonstrated here can only be improved with more photons. The CoMP instrument will continue to be used to investigate outstanding questions regarding the solar corona. Questions requiring measurements at

Figure 11 Histograms of the errors on the LOS magnetic field strength. Solid line: errors inferred from the scatter of the Stokes V signal. Dashed line: error inferred from the distribution of intensity assuming photon noise.
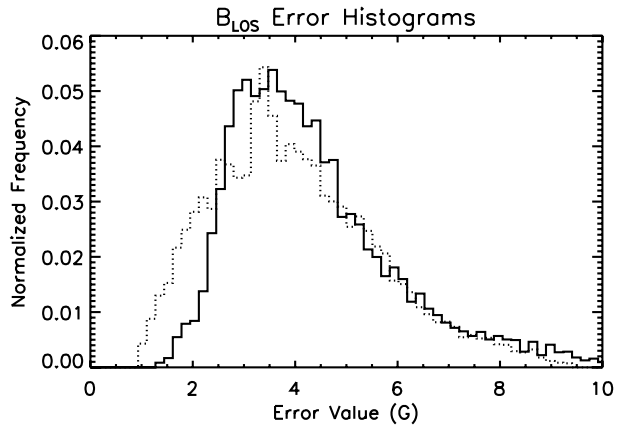
higher spatial and temporal resolutions must await the construction of larger solar coronagraphs than those available today.

References

Arnaud, J., Newkirk, G. Jr.: 1987, *Astron. Astrophys.* **178**, 263.

Babcock, H.A.: 1953, *Astrophys. J.* **118**, 387.

Beckers, J.M., Dunn, R.B.: 1965, AFCRL Technical Report, 65-605.

Billings, B.H.: 1947, *J. Opt. Soc. Am.* **37**, 738.

Bogod, V.M., Gelfreikh, G.B.: 1980, *Solar. Phys.* **67**, 29.

Brosius, J.W., White, S.M.: 2006, *Astrophys. J.* **641**, L69.

Cao, W., Xu, Y., Denker, C., Wang, H.: 2005, In: Longshore, R. (ed.) *Infrared and Photoelectronic Imagers and Detector Devices, Proc. SPIE* **5881**, 245.

Casini, R., Judge, P.G.: 1999, *Astrophys. J.* **522**, 524.

Charvin, P.: 1965, *Ann. d'Astrophys.* **28**, 877.

Evans, J.W.: 1949, *J. Opt. Soc. Am.* **39**, 229.

Gary, D., Hurford, G.J.: 1994, *Astrophys. J.* **420**, 903.

Harvey, J.W.: 1969, Ph.D. Thesis, University of Colorado.

House, L.L.: 1972, *Solar Phys.* **23**, 103.

House, L.L.: 1977, *Astrophys. J.* **214**, 632.

Hyder, C.L.: 1965, *Astrophys. J.* **141**, 1382.

Johnson, B.R.: 1987, *J. Opt. Soc. Am.* **4**, 1376.

Judge, P.G.: 1998, *Astrophys. J.* **500**, 1009.

Judge, P.G., Casini, R., Tomczyk, S., Edwards, D.P., Francis, E.: 2001, NCAR Technical Note, 446+STR.

Judge, P.G., Low, B.C., Casini, R.: 2006, *Astrophys. J.* **651**, 1229.

Kopp, G.: 1994, In: Goldstein, D.H., Chenault, D.B. (eds.) *Polarization, Analysis and Measurement II*, *Proc. SPIE* **2265**, 193.

Kopp, G.A., Derks, M.J., Elmore, D.F., Hassler, D.M., Woods, J.C., Streete, J.L., Blankner, J.G.: 1997, *Appl. Opt.* **36**, 291.

Landi Degl'Innocenti, E.: 1992, In: Sanchez, F., Collados, M., Vázquez, M. (eds.) *Solar Observations: Techniques and Interpretations*, Cambridge University Press, Cambridge, 111.

Lin, H., Penn, M.J., Tomczyk, S.: 2000, *Astrophys. J.* **541**, L83.

Lin, H., Kuhn, J.R., Coulter, R.: 2004, *Astrophys. J.* **613**, L177.

Lyot, B.: 1944, *Ann. Astrophys.* **7**, 31.

Mancuso, S., Spangler, S.R.: 2000, *Astrophys. J.* **539**, 480.

Mickey, D.L.: 1973, *Astrophys. J.* **181**, L19.

Miller, P.: 1990, In: Crawford, D.L. (ed.) *Instrumentation in Astronomy VII*, *Proc. SPIE* **1235**, 466.

Newkirk, G. Jr., Bohlin, D.: 1963, *Appl. Opt.* **2**, 131.

Noll, R.J.: 1973, *J. Opt. Soc. Am.* **63**, 1399.

November, L.J., Wilkins, L.M.: 1992, Phillips Laboratory Technical Report, PL-TR-92-2246.

Öhman, Y.: 1956, *Stockh. Obs. Ann.* **19**, 3.

Penn, M.J., Kuhn, J.R., Arnaud, J., Mickey, D.L., LaBonte, B.J.: 1994, *Space Sci. Rev.* **70**, 185.

Penn, M.J., Lin, H., Tomczyk, S., Elmore, D., Judge, P.: 2004, *Solar. Phys.* **222**, 61.

Ryabov, B.I., Pilyeva, N.A., Alissandrakis, C.E., Shibasaki, K., Bogod, V.M., Garaimov, V.I., Gelfreikh, G.B.: 1999, *Solar Phys.* **185**, 157.

Querfeld, C.W., Smartt, R.N.: 1984, *Solar Phys.* **91**, 299.

Sahal-Bréchot, S.: 1974a, *Astron. Astrophys.* **32**, 147.

Sahal-Bréchot, S.: 1974b, *Astron. Astrophys.* **36**, 355.

Sahal-Bréchot, S.: 1977, *Astrophys. J.* **213**, 887.

Smartt, R.N.: 1979, *Proc. SPIE* **190**, 58.

Smartt, R.N., Dunn, R.B., Fisher, R.R.: 1981, *Proc. SPIE* **288**, 395.

Sofue, Y., Kawabata, K., Takahashi, F., Kawajiri, N.: 1976, *Solar Phys.* **50**, 465.

Staromlynska, J., Rees, S.M., Gillyon, M.P.: 1998, *Appl. Opt.* **37**, 1081.

Stelzried, C.T., Levy, G.S., Sato, T., Rusch, W.V.T., Ohlson, J.E., Schatten, K.H., Wilcox, J.M.: 1970, *Solar Phys.* **14**, 440.

Tarry, H.A.: 1975, *Electron. Lett.* **11**, 471.

Tomczyk, S., McIntosh, S.W., Keil, S.L., Judge, P.G., Schad, T., Seeley, D.H., Edmondson, J.: 2007, *Science* **317**, 1192.

Wang, J., Wang, H., Spirock, T., Lee, C.-Y., Ravindra, N., Ma, J., Goode, P., Denker, C.: 2001, *Opt. Eng.* **40**, 1016.

White, S.M., Kundu, M.R.: 1997, *Solar Phys.* **174**, 31.

Wu, S.T.: 1989, *Appl. Opt.* **28**, 48.